

# A Moving Mesh Method for the Euler Flow Calculations Using a Directional Monitor Function

Hua-Zhong Tang\*

*LMAM, School of Mathematical Sciences, Peking University, Beijing 100871, P.R. China.*

Received 10 July 2005; Accepted (in revised version) 14 November 2005

---

**Abstract.** This paper is concerned with the adaptive grid method for computations of the Euler equations in fluid dynamics. The new feature of the present moving mesh algorithm is the use of a dimensional-splitting type monitor function, which is to increase grid concentration in regions containing shock waves and contact discontinuities or their interactions. Several two-dimensional flow problems are computed to demonstrate the effectiveness of the present adaptive grid algorithm.

**Key words:** Euler equations; adaptive grid method; finite volume method; monitor function.

---

## 1 Introduction

In fluid dynamics, the physical solutions usually develop dynamically singular or nearly singular solutions in fairly localized regions, such as shock waves, detonation waves, contact discontinuities, and boundary layers, etc. To resolve these large solution variations, the numerical simulations may require extremely fine meshes on a small portion of the physical domain. It becomes very expensive for computations of multi-dimensional problems if a uniform mesh is used. It is therefore very necessary to develop an effective, robust, multi-dimensional adaptive grid methods. Successful implementation of the adaptive strategy can increase the accuracy of the numerical approximations and also decrease the computational costs.

Moving mesh methods are a class of adaptive grid methods, which have important applications in fluid dynamics. They include the variational grid methods or adaptive grid generation methods, the traditional Lagrange methods, and their variations such as

---

\*Correspondence to: Hua-Zhong Tang, School of Mathematical Sciences, Peking University, Beijing 100871, P.R. China. Email: [hztang@math.pku.edu.cn](mailto:hztang@math.pku.edu.cn)

arbitrary Lagrangian–Eulerian methods, the free–Lagrange methods, and the unified coordinate system methods. In the past several decades, there has been important progress in moving mesh methods for partial differential equations, including the variational approach of Winslow [33], Brackbill et al. [3, 4], Dvinsky [9], and Li et al. [16, 17]; moving finite element methods of Miller et al. [21], and Davis and Flaherty [8]; and moving mesh PDEs of Cao et al. [6], Li and Petzold [18], and Cenicerros and Hou [7]. We refer the readers to a recent paper [31] for a detailed review. Some recent work on the Lagrange methods can be found in [2, 12, 13, 22] and references therein.

The monitor function is one of the most important issues in the adaptive moving mesh algorithms. The appropriate choice of the monitor will generate grids with good quality in terms of smoothness, skewness, and aspect ratio. Cao et al. [5] gave a general strategy of choosing the monitor function. Some general forms of the monitor function can also be found in [19]. The conventional monitor functions usually depend on the magnitude of the gradient of the solutions, for example,  $\sqrt{1 + \alpha|\rho|^2 + \beta|\nabla\rho|^2}$ . However, the gradient-monitor is not always successful in increasing grid concentration in regions containing shock waves and contact discontinuities or their interactions. Our numerical results will demonstrate this phenomenon. To overcome this drawback, a dimensional–splitting type monitor function will be considered. The moving mesh equations used in this paper is multi–dimensional and more robust than the multidimensional equidistributed methods, see [19].

In this paper, we are interested in developing moving mesh methods based on a variational approach for the hyperbolic conservation laws including the Euler equations of gas dynamics. Harten and Hyman [11] began the earliest study of the self-adaptive moving mesh methods to improve resolution of shock and contact discontinuity. They applied the Godunov method on a non-uniform mesh where the grids move along the characteristic direction. After their work, many other moving mesh methods in this direction have been proposed in the literature based on combining the variational grid methods with high resolution shock capturing methods. They include those of Azarenok et al. [1], Fazio and LeVeque [10], Liu et al. [20], Saleri and Steinberg [23], Stockie et al. [26], and Zegeling [35]. However, it is noticed that many existing moving mesh methods for hyperbolic problems are designed for one space dimension. In 1D, it is generally possible to compute on a very fine grid and so the need for moving mesh methods may not be clear. Multidimensional moving mesh methods are often difficult to be used in fluid dynamics problems since the grid will typically suffer large distortions and possible tangling. It is therefore useful to design a simple and robust moving mesh algorithm for computational problems in fluid dynamics.

Recently, an adaptive moving mesh method for multidimensional hyperbolic conservation laws was proposed by Tang and Tang [28]. The moving mesh algorithm includes two parts: PDE evolution and mesh redistribution. The PDE evolution may be any appropriate high resolution finite volume scheme. The mesh redistribution is an iterative procedure. In each time iteration, grid points are first redistributed by a variational principle, and then the numerical solutions are updated on the resulting new meshes by a

*conservative–interpolation* formula.

This paper is to continue the study of [28]. The new feature of the present method is to use a dimensional-splitting type monitor function to increase grid concentration in regions containing shock waves and contact discontinuities or their interactions. This monitor is defined based on an observation of our mesh generation equations. We will also give numerical comparisons and computations of several two-dimensional flow problems to demonstrate the effectiveness of the present moving mesh algorithm in improving resolution of the discontinuities and in increasing grid concentration in the regions containing the discontinuities.

The paper is organized as follows. In Section 2, we present our moving mesh algorithm. Section 2.1 gives the mesh–redistribution strategy based on a variational principle using a new monitor function. Although the new monitor is based on dimensional splitting in the logic space, our moving mesh methods are different from the existing multidimensional equidistribution schemes mentioned in [19]. Section 2.2 reviews the derivation of a *conservative–interpolation* formula for solution–updating on new meshes. The PDEs evolution is described in Section 2.3. The detailed solution procedure is outlined in Section 2.4. Section 2.5 gives a simple implementation of the boundary mesh motion in the physical domain, which will be used in our computations. Numerical experiments and comparisons are carried out in Section 3, where several 2D examples are considered. We conclude this work in Section 4.

## 2 An adaptive moving mesh method

Consider multi-dimensional hyperbolic conservation laws

$$\frac{\partial U}{\partial t} + \sum_{i=1}^d \frac{\partial F_i(U)}{\partial x_i} = H(\vec{x}, U), \quad 0 < t \leq T, \quad (2.1)$$

subject to the initial data  $U(\vec{x}, 0) = U_0(\vec{x})$ , where  $T$  is a finite number,  $d$  denotes the number of spatial dimensions,  $\vec{x} = (x_1, \dots, x_d)$ ,  $U$  and  $F_i(U)$  denote a conservative variable and flux in  $x_i$ -direction, respectively, and  $H(\vec{x}, U)$  is a source term. A typical example of the above equation (2.1) are the Euler equations (3.1).

For convenience, we will restrict our attention to  $d = 2$  throughout this paper. Given a partition  $\{A_{j+\frac{1}{2}, k+\frac{1}{2}}\}$  of the physical domain  $\Omega_p$ , where  $A_{j+\frac{1}{2}, k+\frac{1}{2}}$  is a quadrangle with four vertices  $\vec{x}_{j+p, k+q}$ ,  $p, q \in \{0, 1\}$ , as shown in Fig. 1.

The initial data is approximated by a cell average:

$$U_{j+\frac{1}{2}, k+\frac{1}{2}}^0 = \frac{1}{|A_{j+\frac{1}{2}, k+\frac{1}{2}}|} \int_{A_{j+\frac{1}{2}, k+\frac{1}{2}}} U_0(\vec{x}) \, d\vec{x}, \quad (2.2)$$

where  $|A_{j+\frac{1}{2}, k+\frac{1}{2}}|$  denotes the area of the control volume  $A_{j+\frac{1}{2}, k+\frac{1}{2}}$ .

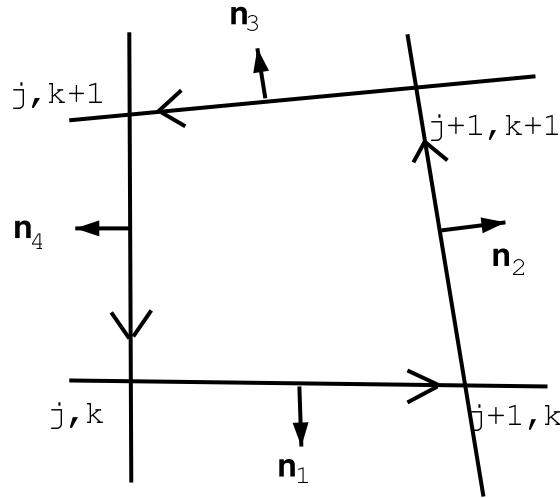


Figure 1: A 2D finite control volume  $A_{j+\frac{1}{2}, k+\frac{1}{2}}$ .

Our adaptive moving mesh methods will contain the following steps: Mesh-redistribution based on variational methods (Section 2.1); conservative solution-updating on new meshes (Section 2.2); and evolution of the governing equations (Section 2.3). The complete solution procedure will be briefly outlined in Section 2.4.

### 2.1 Mesh-redistribution

The calculus of variations has been proved to provide an excellent opportunity to create new techniques for generation of grids or mesh-redistribution by utilizing the idea of optimization of grid characteristics modeled through appropriate functionals. The grid characteristics include grid smoothness, cell skewness, cell volume, and departure from orthogonality of conformality. We refer the readers to [3, 4, 9, 19, 33] and references therein for details.

In our calculus of variations, the functional is defined by the integral

$$E[\vec{x}] = \int_{\Omega_c} \mathcal{G}(\vec{\xi}, \vec{x}, \vec{x}_{\xi_l}, \vec{x}_{\xi_l \xi_m}) d\vec{\xi}, \tag{2.3}$$

where  $\vec{\xi} = (\xi_1, \dots, \xi_d)$  is the logical (or computational) coordinates,  $\Omega_c$  is a logical domain,  $\vec{x}_{\xi_l}$  and  $\vec{x}_{\xi_l \xi_m}$  are first- and second-order partial derivatives of  $\vec{x}$  with respect to  $\xi_l$ . An optimal transformation  $\vec{x} = \vec{x}(\vec{\xi})$  for the functional (2.3) is the solution of the following system of the Euler-Lagrange equations

$$\mathcal{G}_{x_i} - \frac{\partial}{\partial \xi_l} \mathcal{G}_{\frac{\partial x_i}{\partial \xi_l}} + \frac{\partial^2}{\partial \xi_l \partial \xi_m} \mathcal{G}_{\frac{\partial^2 x_i}{\partial \xi_l \partial \xi_m}} = 0, \quad i = 1, \dots, d, \tag{2.4}$$

defined in the interior of the domain  $\Omega_c$ , where subscripts  $x_i$ ,  $\frac{\partial x_i}{\partial \xi_l}$ , and  $\frac{\partial^2 x_i}{\partial \xi_l \partial \xi_m}$  are the corresponding partial derivatives of  $\mathcal{G}$ . Usually,  $\mathcal{G}$  can be taken as

$$\mathcal{G} = \sum_{i=1}^d (\tilde{\nabla} x_i)^T G_i \tilde{\nabla} x_i, \quad (2.5)$$

where  $\tilde{\nabla} = (\partial_{\xi_1}, \dots, \partial_{\xi_d})^T$ , and  $G_i$  are given symmetric positive definite matrices, called *monitor functions*. In general, the monitor functions depend on the underlying solution to be adapted. It is very important to choose a suitable monitor function for a moving mesh algorithm in order to increase the concentration of grid points in a desired localized region, or improve the quality of the adaptive meshes. If  $\mathcal{G}$  is of the form (2.5), then (2.4) becomes

$$\tilde{\nabla} \cdot (G_i \tilde{\nabla} x_i) = 0, \quad i = 1, \dots, d. \quad (2.6)$$

Solving the Euler–Lagrange equations (2.6) on  $\Omega_c$  will give directly a coordinate transformation  $\vec{x} = \vec{x}(\vec{\xi})$  from the logical domain  $\Omega_c$  to the physical domain  $\Omega_p$ . Solving the mesh equation (2.6) is not difficult, since it is defined in the logical domain which in most cases is chosen as a unit square.

In this paper,  $G_i$  will be taken as

$$G = \text{diag}\{w_1, \dots, w_d\}, \quad (2.7)$$

and (2.6) is further reduced to

$$\frac{\partial}{\partial \xi_1} \left( w_1 \frac{\partial x_i}{\partial \xi_1} \right) + \dots + \frac{\partial}{\partial \xi_d} \left( w_d \frac{\partial x_i}{\partial \xi_d} \right) = 0, \quad i = 1, \dots, d. \quad (2.8)$$

The control function  $w_l$  is traditionally defined by

$$w_l \equiv w = \left( 1 + \alpha |\psi|^2 + \beta \sum_{i=1}^d \left| \frac{\partial \psi}{\partial \xi_i} \right|^2 \right)^{\frac{\gamma}{2}}, \quad 1 \leq l \leq d, \quad (2.9)$$

where  $\alpha$ ,  $\beta$  and  $\gamma$  are user-defined positive constants, and  $\psi$  denotes one of the dependent variables, e.g.,  $\psi = \psi(\rho, u, p)$ .

The monitor function (2.9) means that the function  $w_l$  depends on variations of the gradient of the underlying solution  $\psi$  in all coordinate directions. However, we may find from (2.8) that  $w_l$  only plays a role to control the movement of a grid point in the  $\xi_l$ -direction in the logical space. Therefore, if there is no variation of the gradient for the underlying solution in the  $\xi_l$ -direction, then it is expected that the grid points should keep almost unchanged in that direction.

Based on this observation, another control function  $w_l$  can be defined by

$$w_l = \left( 1 + \alpha_l |\psi|^2 + \beta_l \left| \frac{\partial \psi}{\partial \xi_l} \right|^2 \right)^{\frac{\gamma_l}{2}}, \quad l = 1, \dots, d, \quad (2.10)$$

where  $\alpha_l, \beta_l$  and  $\gamma_l$  are some positive constants. For convenience, we will use  $G$  and  $\widehat{G}$  to denote the monitor function (2.7) with (2.9) and (2.10), respectively. The monitor function  $\widehat{G}$  will affect mainly the grid node redistribution in the direction of the logical coordinate lines. Although the monitor  $\widehat{G}$  is given based on an idea of dimensional splitting type methods, our moving mesh equations are still different from the existing multidimensional equidistribution. The latter is to just simply generate the adaptive meshes by tensor-type extension of the one-dimensional equidistribution algorithm.

Before ending this subsection, we give a finite difference or volume discretization of the mesh equation (2.8). In the remainder of this work, we will concentrate on two-dimensional computations. Divide the logical domain  $\Omega_c = \{(\xi_1, \xi_2) = (\xi, \eta) | 0 \leq \xi \leq 1, 0 \leq \eta \leq 1\}$  into the square mesh cells:

$$\left\{ (\xi_j, \eta_k) \mid \xi_j = j\Delta\xi, \eta_k = k\Delta\eta; 0 \leq j \leq N_x + 1, 0 \leq k \leq N_y + 1 \right\},$$

where  $\Delta\xi = 1/(N_x + 1)$  and  $\Delta\eta = 1/(N_y + 1)$ . Correspondingly, the numerical approximations to  $\vec{x} = \vec{x}(\xi, \eta)$  are denoted by  $\vec{x}_{j,k} = \vec{x}(\xi_j, \eta_k)$ . The Euler-Lagrange equation (2.6) is discretized by a second-order central difference scheme as

$$\frac{\Delta_-^j ((w_1)_{j+\frac{1}{2},k} \Delta_+^j (x_i)_{j,k})}{(\Delta\xi)^2} + \frac{\Delta_-^k ((w_2)_{j,k+\frac{1}{2}} \Delta_+^k (x_i)_{j,k})}{(\Delta\eta)^2} = 0, \tag{2.11}$$

where  $\Delta_+^\nu$  and  $\Delta_-^\nu$  denote forward and backward difference operators respectively in  $\xi$ -direction when  $\nu = j$ , and  $\eta$ -direction when  $\nu = k$ , and

$$\begin{aligned} (w_1)_{j+\frac{1}{2},k} &= \frac{1}{2}((w_1)_{j+\frac{1}{2},k+\frac{1}{2}} + (w_1)_{j+\frac{1}{2},k-\frac{1}{2}}), \\ (w_2)_{j,k+\frac{1}{2}} &= \frac{1}{2}((w_2)_{j+\frac{1}{2},k+\frac{1}{2}} + (w_2)_{j-\frac{1}{2},k+\frac{1}{2}}). \end{aligned}$$

The discrete system (2.11) with Dirichlet boundary condition can be solved by some explicit iteration methods, e.g., Gauss-Seidel (G-S) iteration, with a fixed number of iterations.

In [28], the monitor function  $G$  given in (2.7) with (2.9) is used. The results showed that a unsatisfactory resolution was obtained for contact discontinuities. This is the main motivation for suggesting the new monitor (2.7) with (2.10). Moreover, the G-S iteration method will be applied in our computations. It is found that G-S iteration is much more robust than the Jacobi iteration, even though the latter has a good symmetry.

## 2.2 Conservative solution interpolation

Let  $\vec{x}_{j,k}$  and  $\widetilde{\vec{x}}_{j,k}$  be the coordinates of the old and new grid points, respectively, in the sense that the grid point  $\vec{x}_{j,k}$  will move to position  $\widetilde{\vec{x}}_{j,k}$  after one G-S iteration for the mesh equations. Use  $A_{j+\frac{1}{2},k+\frac{1}{2}}$  and  $\widetilde{A}_{j+\frac{1}{2},k+\frac{1}{2}}$  to denote the quadrangles (finite control

volumes) with four vertices  $(\vec{x}_{j+p,k+q})$ , and  $(\vec{\tilde{x}}_{j+p,k+q})$ ,  $p, q \in \{0, 1\}$ , respectively. They are of similar setup to the one shown in Fig.1.

Using a perturbation method, we can derive a *conservative* interpolation scheme to update cell average values  $\tilde{U}_{j+\frac{1}{2},k+\frac{1}{2}}$  on the control volume  $\tilde{A}_{j+\frac{1}{2},k+\frac{1}{2}}$ . Assuming  $(\tilde{x}, \tilde{y}) = (x - c^x(x, y), y - c^y(x, y))$  with small magnitudes of speed  $(c^x, c^y)$ , we have

$$\begin{aligned} \int_{\tilde{A}_{j+\frac{1}{2},k+\frac{1}{2}}} U(\tilde{x}, \tilde{y}) \, d\tilde{x}d\tilde{y} &= \int_{A_{j+\frac{1}{2},k+\frac{1}{2}}} U(x - c^x, y - c^y) \det \left( \frac{\partial(\tilde{x}, \tilde{y})}{\partial(x, y)} \right) \, dxdy \quad (2.12) \\ &\approx \int_{A_{j+\frac{1}{2},k+\frac{1}{2}}} (U(x, y) - c^x U_x - c^y U_y)(1 - c^x - c^y) \, dxdy \\ &\approx \int_{A_{j+\frac{1}{2},k+\frac{1}{2}}} [U(x, y) - (c^x U)_x - (c^y U)_y] \, dxdy \\ &\approx \int_{A_{j+\frac{1}{2},k+\frac{1}{2}}} U(x, y) \, dxdy - [(c_{\vec{n}}^2 U)_{j+1,k+\frac{1}{2}} + (c_{\vec{n}}^4 U)_{j,k+\frac{1}{2}}] - [(c_{\vec{n}}^3 U)_{j+\frac{1}{2},k+1} + (c_{\vec{n}}^1 U)_{j+\frac{1}{2},k}], \end{aligned}$$

where the higher order terms have been neglected,  $c_{\vec{n}}^l := c^x n_x^l + c^y n_y^l$  with the normal outward vector  $\vec{n}^l = (n_x^l, n_y^l)$  defined as follows:

$$\begin{aligned} c_{\vec{n}}^1 &= \frac{1}{2}(c_{j,k}^x + c_{j+1,k}^x)(y_{j+1,k} - y_{j,k}) - \frac{1}{2}(c_{j,k}^y + c_{j+1,k}^y)(x_{j+1,k} - x_{j,k}), \\ c_{\vec{n}}^2 &= \frac{1}{2}(c_{j+1,k}^x + c_{j+1,k+1}^x)(y_{j+1,k+1} - y_{j+1,k}) - \frac{1}{2}(c_{j+1,k}^y + c_{j+1,k+1}^y)(x_{j+1,k+1} - x_{j+1,k}), \\ c_{\vec{n}}^3 &= \frac{1}{2}(c_{j+1,k+1}^x + c_{j,k+1}^x)(y_{j,k+1} - y_{j+1,k+1}) - \frac{1}{2}(c_{j+1,k+1}^y + c_{j,k+1}^y)(x_{j,k+1} - x_{j+1,k+1}), \\ c_{\vec{n}}^4 &= \frac{1}{2}(c_{j,k+1}^x + c_{j,k}^x)(y_{j,k} - y_{j,k+1}) - \frac{1}{2}(c_{j,k+1}^y + c_{j,k}^y)(x_{j,k} - x_{j,k+1}), \end{aligned}$$

and  $(c_{\vec{n}} U)_{j+p,k+\frac{1}{2}}$  and  $(c_{\vec{n}} U)_{j+\frac{1}{2},k+q}$ ,  $p, q = 0$  or  $1$ , denote the values of  $c_{\vec{n}} U$  on the corresponding surface of the control volume  $A_{j+\frac{1}{2},k+\frac{1}{2}}$ . They will be approximated by using an upwind scheme. For example, the term  $(c_{\vec{n}} U)_{j+1,k+\frac{1}{2}}$  may be approximated by

$$(c_{\vec{n}} U)_{j+1,k+\frac{1}{2}} = \frac{c_{\vec{n}}^2}{2}(U_{j+\frac{3}{2},k+\frac{1}{2}} + U_{j+\frac{1}{2},k+\frac{1}{2}}) - \frac{|c_{\vec{n}}^2|}{2}(U_{j+\frac{3}{2},k+\frac{1}{2}} - U_{j+\frac{1}{2},k+\frac{1}{2}}). \quad (2.13)$$

The above approximation is only first-order accurate in space. In order to avoid large numerical dissipation, we will use the reconstruction technique proposed in [32], which will be described in Section 2.3.

From (2.12), a conservative-interpolation formula is obtained:

$$\begin{aligned} |\tilde{A}_{j+\frac{1}{2},k+\frac{1}{2}}| \tilde{U}_{j+\frac{1}{2},k+\frac{1}{2}} &= |A_{j+\frac{1}{2},k+\frac{1}{2}}| U_{j+\frac{1}{2},k+\frac{1}{2}} \\ &\quad - [(c_{\vec{n}}^2 U)_{j+1,k+\frac{1}{2}} + (c_{\vec{n}}^4 U)_{j,k+\frac{1}{2}}] - [(c_{\vec{n}}^3 U)_{j+\frac{1}{2},k+1} + (c_{\vec{n}}^1 U)_{j+\frac{1}{2},k}], \end{aligned} \quad (2.14)$$

where  $|\tilde{A}|$  and  $|A|$  denote the areas of the control volumes  $\tilde{A}$  and  $A$ , respectively. It can be verified that the above interpolation scheme satisfies the following mass-conservation property:

$$\sum_{j,k} |\tilde{A}_{j+\frac{1}{2},k+\frac{1}{2}}| \tilde{U}_{j+\frac{1}{2},k+\frac{1}{2}} = \sum_{j,k} |A_{j+\frac{1}{2},k+\frac{1}{2}}| U_{j+\frac{1}{2},k+\frac{1}{2}}. \tag{2.15}$$

It is also possible to derive a conservative-interpolation from a geometric point of view. For the one-dimensional case, we have

$$\int_{\tilde{x}_j}^{\tilde{x}_{j+1}} U(x) dx = \int_{x_j}^{x_{j+1}} U(x) dx + \left( \int_{\tilde{x}_j}^{x_j} U(x) dx - \int_{\tilde{x}_{j+1}}^{x_{j+1}} U(x) dx \right),$$

i.e.

$$(\tilde{x}_{j+1} - \tilde{x}_j) \tilde{U}_{j+\frac{1}{2}} = (x_{j+1} - x_j) U_{j+\frac{1}{2}} + \left( \int_{\tilde{x}_j}^{x_j} U(x) dx - \int_{\tilde{x}_{j+1}}^{x_{j+1}} U(x) dx \right).$$

According to the locations of the new points  $\tilde{x}_j$  and  $\tilde{x}_{j+1}$ , we can give a suitable approximation for the last two integrals, which leads to the conservative-interpolation formula as proposed in [28]. However, it will become very complicated to construct multidimensional conservative-interpolation using this geometrical approach, although we believe that multidimensional conservative-interpolation obtained by using the geometrical approach is more accurate and more suitable than (2.14) in solving the complex problems.

### 2.3 PDE evolution

Assume that a partition  $\vec{x}_{j,k} = (x_{j,k}, y_{j,k})$  of the physical domain  $\Omega_p$  is given, and the initial data  $U_{j+\frac{1}{2},k+\frac{1}{2}}^0$  is defined by (2.2). Integrating (2.1) over the finite control volume  $A_{j+\frac{1}{2},k+\frac{1}{2}}$  gives

$$\frac{\partial}{\partial t} \iint_{A_{j+\frac{1}{2},k+\frac{1}{2}}} U dx dy + \sum_{l=1}^4 F_{\vec{n}^l}(U)|_{(x,y) \in s_i} = \iint_{A_{j+\frac{1}{2},k+\frac{1}{2}}} H dx dy, \tag{2.16}$$

where  $s_i, i = 1, 2, 3, 4$ , are four sides of  $A_{j+\frac{1}{2},k+\frac{1}{2}}$ ,  $F_{\vec{n}^l} = \vec{F} \cdot \vec{n}^l$ , and  $\vec{n}^l = (n_x^l, n_y^l)$  are the normal outward vectors, defined as

$$\begin{aligned} \vec{n}^1 &= (y_{j+1,k} - y_{j,k}, x_{j,k} - x_{j+1,k}), & \vec{n}^2 &= (y_{j+1,k+1} - y_{j+1,k}, x_{j+1,k} - x_{j+1,k+1}), \\ \vec{n}^3 &= (y_{j,k+1} - y_{j+1,k+1}, x_{j+1,k+1} - x_{j,k+1}), & \vec{n}^4 &= (y_{j,k} - y_{j,k+1}, x_{j,k+1} - x_{j,k}). \end{aligned}$$

By assuming  $F_{\vec{n}^l} = F_{\vec{n}^l}^+ + F_{\vec{n}^l}^-$ , we obtain a first-order finite volume scheme for (2.1):

$$\begin{aligned} U_{j+\frac{1}{2},k+\frac{1}{2}}^{n+1} &= U_{j+\frac{1}{2},k+\frac{1}{2}}^n - \frac{\Delta t}{|A_{j+\frac{1}{2},k+\frac{1}{2}}|} \left( \sum_{l=1}^4 F_{\vec{n}^l}^+(U_{j+\frac{1}{2},k+\frac{1}{2}}^n) + F_{\vec{n}^1}^-(U_{j+\frac{1}{2},k-\frac{1}{2}}^n) \right. \\ &\quad \left. + F_{\vec{n}^2}^-(U_{j+\frac{3}{2},k+\frac{1}{2}}^n) + F_{\vec{n}^3}^-(U_{j+\frac{1}{2},k+\frac{3}{2}}^n) + F_{\vec{n}^4}^-(U_{j-\frac{1}{2},k+\frac{1}{2}}^n) \right) + \Delta t H_{j+\frac{1}{2},k+\frac{1}{2}}^n. \end{aligned} \tag{2.17}$$



The spatial accuracy of the scheme (2.17) can be improved by using the reconstruction technique. Following [32], we use the piecewise linear function

$$\bar{U}_{j+\frac{1}{2},k+\frac{1}{2}}^n(x,y) = U_{j+\frac{1}{2},k+\frac{1}{2}}^n + \vec{S}_{j+\frac{1}{2},k+\frac{1}{2}}^n \cdot (\vec{x} - \vec{x}_{j+\frac{1}{2},k+\frac{1}{2}}), \quad (x,y) \in A_{j+\frac{1}{2},k+\frac{1}{2}}, \quad (2.18)$$

to replace the piecewise constant function  $U_{j+\frac{1}{2},k+\frac{1}{2}}^n$  at each time level  $t_n$ , where  $\vec{S}_{j+\frac{1}{2},k+\frac{1}{2}}^n$  is an approximation of the gradient  $\nabla U$ . This gives a second-order scheme:

$$\begin{aligned} U_{j+\frac{1}{2},k+\frac{1}{2}}^{n+1} = & U_{j+\frac{1}{2},k+\frac{1}{2}}^n - \frac{\Delta t}{|A_{j+\frac{1}{2},k+\frac{1}{2}}|} \left( \sum_{l=1}^4 F_{\vec{n}^l}^+(\bar{U}_{j+\frac{1}{2},k+\frac{1}{2}}^n(\vec{x}_{c^l})) + F_{\vec{n}^1}^-(\bar{U}_{j+\frac{1}{2},k-\frac{1}{2}}^n(\vec{x}_{c^1})) \right. \\ & \left. + F_{\vec{n}^2}^-(\bar{U}_{j+\frac{3}{2},k+\frac{1}{2}}^n(\vec{x}_{c^2})) + F_{\vec{n}^3}^-(\bar{U}_{j+\frac{1}{2},k+\frac{3}{2}}^n(\vec{x}_{c^3})) + F_{\vec{n}^4}^-(\bar{U}_{j-\frac{1}{2},k+\frac{1}{2}}^n(\vec{x}_{c^4})) \right) \\ & + \Delta t H_{j+\frac{1}{2},k+\frac{1}{2}}^n =: U_{j+\frac{1}{2},k+\frac{1}{2}}^n + \Delta t L_{j+\frac{1}{2},k+\frac{1}{2}}(U^n), \end{aligned} \quad (2.19)$$

where  $\vec{x}_{c^l}$  denotes the coordinates of the midpoint of the  $l$ th edge of the control element  $A_{j+\frac{1}{2},k+\frac{1}{2}}$ .

In our computations, the van Leer’s slope limiter is used to suppress the appearance of numerical oscillations. Moreover, the second-order TVD Runge-Kutta time discretization [25]

$$U_{j+\frac{1}{2},k+\frac{1}{2}}^* = U_{j+\frac{1}{2},k+\frac{1}{2}}^n + \Delta t L_{j+\frac{1}{2},k+\frac{1}{2}}(U^n), \quad (2.20)$$

$$U_{j+\frac{1}{2},k+\frac{1}{2}}^{n+1} = \frac{1}{2} (U_{j+\frac{1}{2},k+\frac{1}{2}}^n + U_{j+\frac{1}{2},k+\frac{1}{2}}^* + \Delta t L_{j+\frac{1}{2},k+\frac{1}{2}}(U^*)), \quad (2.21)$$

is used to replace the forward Euler time discretization (2.19).

**Remark 2.1.** In practice, we may simplify the problem in question by applying the initial reconstruction technique along each normal direction of the finite control volume.

### 2.4 Solution procedure

The solution procedure of our adaptive mesh strategy for two-dimensional hyperbolic problems can be summarized as follows:

**Step i** Give an initial partition  $\vec{x}_{j,k}^{[0]} = (x_{j,k}^{[0]}, y_{j,k}^{[0]}) := (x_{j,k}, y_{j,k})$  of the physical domain  $\Omega_p$  and a uniform (fixed) partition of the logical domain  $\Omega_c$ , and compute grid values  $U_{j+\frac{1}{2},k+\frac{1}{2}}^{[0]}$  by cell average over control volume  $A_{j+\frac{1}{2},k+\frac{1}{2}}^{[0]}$  based on the initial data  $U(\vec{x}, 0)$ .

**Step ii** For  $\nu = 0, 1, 2, \dots, M$ , with  $M$  a fixed number, do the following:

- (a). Move grid points  $\vec{x}_{j,k}^{[\nu]}$  to  $\vec{x}_{j,k}^{[\nu+1]}$  by solving (2.11) with one Gauss–Seidel iteration.
- (b). Compute  $\{U_{j+\frac{1}{2},k+\frac{1}{2}}^{[\nu+1]}\}$  over the new control volume  $A_{j+\frac{1}{2},k+\frac{1}{2}}^{[\nu+1]}$  using the conservative-interpolation (2.14).

Step iii Evolve the underlying PDEs by using 2D high-resolution finite volume methods given in Section 2.3 on the mesh  $\vec{x}_{j,k}^{[M+1]}$  to obtain the numerical approximations  $U_{j+\frac{1}{2},k+\frac{1}{2}}^{n+1}$  at the time level  $t_{n+1}$ .

Step iv If  $t_{n+1} < T$ , then let  $U_{j+\frac{1}{2},k+\frac{1}{2}}^{[0]} := U_{j+\frac{1}{2},k+\frac{1}{2}}^{n+1}$  and  $\vec{x}_{j,k}^{[0]} := \vec{x}_{j,k}^{[M+1]}$ , and go to Step ii.

### 2.5 Boundary redistribution

In practical flow situations, the discontinuities may initially exist in boundaries or move to boundaries at later times. As a consequence, movement of boundary points should be made possible in order to improve the quality of the adaptive solutions near the boundary. A simple redistribution strategy is proposed as follows. For convenience, our attention is restricted to the case where the physical domain  $\Omega_p$  is rectangular. Assume a new set of grid points  $\vec{\tilde{x}}_{j,k}$  is obtained in  $\Omega_p$  by solving the moving mesh equation (2.11). Then the speeds of the internal grid points  $\vec{c}_{j,k}$  are given by

$$(c^x, c^y)_{j,k} := (x^{[\nu]} - x^{[\nu+1]}, y^{[\nu]} - y^{[\nu+1]})_{j,k}, \quad \text{for } 1 \leq j \leq N_x, 1 \leq k \leq N_y.$$

We assume that the points on the boundaries are moving with the same speed as the tangential components of the speed for the internal points adjacent to those boundary points, namely

$$\begin{aligned} (c^x, c^y)_{0,k} &= (0, c_{1,k}^y), & (c^x, c^y)_{N_x+1,k} &= (0, c_{N_x,k}^y), & 1 \leq k \leq N_y, \\ (c^x, c^y)_{j,0} &= (c_{j,1}^x, 0), & (c^x, c^y)_{j,N_y+1} &= (c_{j,N_y}^x, 0), & 1 \leq j \leq N_x. \end{aligned}$$

Thus, the new boundary points  $\vec{\tilde{x}}_{0,k}$ ,  $\vec{\tilde{x}}_{N_x+1,k}$ ,  $\vec{\tilde{x}}_{j,0}$  and  $\vec{\tilde{x}}_{j,N_y+1}$  are defined by

$$\begin{aligned} (\tilde{x}, \tilde{y})_{j,k} &= (x, y)_{j,k} - (c^x, c^y)_{j,k}, & j = 0 \text{ or } N_x + 1, & 1 \leq k \leq N_y, \\ (\tilde{x}, \tilde{y})_{j,k} &= (x, y)_{j,k} - (c^x, c^y)_{j,k}, & 1 \leq j \leq N_x, & k = 0 \text{ or } N_y + 1. \end{aligned}$$

Numerical experiments show that the above procedure to move the boundary points is useful in improving the solution resolution.

If the physical domain  $\Omega_p$  is not a rectangular, then we introduce an intermediate or parameter space  $\mathcal{D}$  with Cartesian coordinates  $\vec{\zeta} = (\zeta_1, \zeta_2)$  where  $\mathcal{D}$  is taken as the unit square. At  $t = 0$ , we construct an initial map  $\vec{x} = \vec{x}(\vec{\zeta}) : \mathcal{D} \rightarrow \Omega_p$  by calculus of variations or using an algebraic grid generation method, if there does not exist any map between  $\Omega_p$  and  $\mathcal{D}$  with an explicit algebraic expression. For  $t > 0$ , we first move the grid points in  $\mathcal{D}$  according to the previous algorithm, i.e. to solve the following moving mesh equations

$$\frac{\Delta_-^j((w_1)_{j+\frac{1}{2},k} \Delta_+^j(\zeta_i)_{j,k})}{(\Delta \xi)^2} + \frac{\Delta_-^k((w_2)_{j,k+\frac{1}{2}} \Delta_+^k(\zeta_i)_{j,k})}{(\Delta \eta)^2} = 0, \quad i = 1, 2. \tag{2.22}$$

Next we update the underlying solutions by using the conservative-interpolation formula given in Section 2.2, and the Cartesian coordinates  $\vec{x}$  in  $\Omega_p$  by a non-conservative high resolution interpolation used in [30], i.e, using a high resolution scheme to solve the following discrete equation:

$$\vec{x}(\vec{\zeta}) = \vec{x}(\vec{\zeta}) + (\vec{\zeta} - \vec{\zeta}) \cdot \nabla_{\vec{\zeta}} \vec{x}. \quad (2.23)$$

Here  $\vec{x}$  is considered as the functions of  $\vec{\zeta}$ , and  $\vec{x}_{j,k}$  is the nodal discretization. In order to give a map  $\vec{x} = \vec{x}(\vec{\zeta})$ , using a non-conservation interpolation (2.23) instead of the mesh generation procedure may save the computational cost.

The idea of introducing an intermediate space has also been widely used in numerical grid generations, see e.g., [19,27] for details.

### 3 Numerical experiments

In this section, we solve the Euler equations governing two-dimensional inviscid compressible fluid flows,

$$\frac{\partial}{\partial t} \begin{pmatrix} \rho \\ \rho u \\ \rho v \\ E \end{pmatrix} + \frac{\partial}{\partial x} \begin{pmatrix} \rho u \\ \rho u^2 + p \\ \rho uv \\ u(E + p) \end{pmatrix} + \frac{\partial}{\partial y} \begin{pmatrix} \rho v \\ \rho vu \\ \rho v^2 + p \\ v(E + p) \end{pmatrix} = 0, \quad (3.1)$$

where  $\rho$  is the density,  $(u, v)$  is the velocity vector,  $E$  is the total energy,  $p$  is the pressure. Assume that the pressure is related to the total energy by  $E = \frac{p}{\gamma-1} + \frac{1}{2}\rho(u^2 + v^2)$  with  $\gamma = 1.4$ . The physical fluxes are approximated by the kinetic flux-vector splitting method. For example, the flux  $(F_1)_{j,k+\frac{1}{2}}$  in  $x$ -direction can be approximated by

$$(F_1)_{j,k+\frac{1}{2}} = (F_1)_{j-\frac{1}{2},k+\frac{1}{2}}^+ + (F_1)_{j+\frac{1}{2},k+\frac{1}{2}}^-,$$

$$(F_1)^\pm = \left( \rho[\tilde{u}^1]_\pm, \rho[\tilde{u}^2]_\pm, \rho[\tilde{u}]_\pm[\tilde{v}^1], \frac{1}{2}([\tilde{u}^3]_\pm + [\tilde{u}]_\pm[\xi^2]) \right)^T,$$

where

$$[\tilde{v}^1] = v, \quad [\xi^2] = \frac{K}{2\lambda},$$

$$[\tilde{u}^0]_\pm = \frac{1}{2} \operatorname{erfc}(\mp \sqrt{\lambda} u), \quad [\tilde{u}^1]_\pm = u[\tilde{u}^0]_\pm \pm \frac{e^{-\lambda u^2}}{\sqrt{\pi \lambda}},$$

$$[\tilde{u}^{n+2}]_\pm = u[\tilde{u}^{n+1}]_\pm + \frac{n+1}{2\lambda} [\tilde{u}^n]_\pm, \quad n \geq 0.$$

Here  $\lambda = \rho/2p$ ,  $K = -2 + 2/(\gamma - 1)$  and  $\operatorname{erfc}(x)$  denotes the complementary error function.

In the following, we will apply the moving mesh algorithm described in Section 2.4 to our numerical experiments, and compare the monitor function  $\widehat{G}$  defined in (2.7) with

(2.10) to the monitor function  $G$  with (2.9). Unless otherwise specified, the number of G-S iteration for the mesh equations is taken as 5;  $\alpha_l = \alpha = 0$ . Throughout the computations, the CFL number used is 0.24. The computations are run on PC Pentium-III with 800 MHz.

**Example 3.1.** 2D Riemann problem I: shock waves [15, 24].

The initial data are chosen as

$$W(x, y, 0) = \begin{cases} (1.1, 0.0, 0.0, 1.1) & \text{if } x > 0.5, \quad y > 0.5, \\ (0.5065, 0.8939, 0.0, 0.35) & \text{if } x < 0.5, \quad y > 0.5, \\ (1.1, 0.8939, 0.8939, 1.1) & \text{if } x < 0.5, \quad y < 0.5, \\ (0.5065, 0.0, 0.8939, 0.35) & \text{if } x > 0.5, \quad y < 0.5, \end{cases}$$

which corresponds to the case of left forward shock, right backward shock, upper backward shock, and lower forward shock,  $W = (\rho, u, v, p)^T$ . We refer the readers to [15, 24] for details.

Fig. 2 shows the adaptive meshes with  $50 \times 50$  grid points at  $t = 0.25$  obtained by using two monitor functions (2.9) and (2.10) with  $\beta_l = \beta = 8$  and  $\gamma_l = \gamma = 1$ , respectively. It is observed that using the monitor function  $\widehat{G}$  can increase grid concentration in shock curves and in particular near two shock interaction points (0.92, 0.3) and (0.3, 0.92). Figs. 3 and 4 show the adaptive meshes and fluid density at  $t = 0.25$  with  $50 \times 50$  grid points, obtained by  $G$  and  $\widehat{G}$  with  $\beta_l = \beta = 8$  and  $\gamma_l = \gamma = \frac{3}{2}$ , respectively. A sharper shock resolution and a better grid concentration are obtained by using  $\widehat{G}$ . The results in Fig. 4 have almost the same resolution as the ones given in [28] with the monitor function  $G$  and  $100 \times 100$  grid points.

**Example 3.2.** 2D Riemann problem II: contact discontinuities [15, 24].

The initial data are chosen as

$$W(x, y, 0) = \begin{cases} (1, 0.75, -0.5, 1) & \text{if } x > 0.5, \quad y > 0.5, \\ (2, 0.75, 0.5, 1) & \text{if } x < 0.5, \quad y > 0.5, \\ (1, -0.75, 0.5, 1) & \text{if } x < 0.5, \quad y < 0.5, \\ (3, -0.75, -0.5, 1) & \text{if } x > 0.5, \quad y < 0.5, \end{cases}$$

which corresponds to the case of left forward contact, right backward contact, upper backward contact, and lower forward contact. The purpose of computing this problem is to test the ability of our adaptive moving mesh algorithm in resolving contact discontinuities. Fig. 5 shows the adaptive meshes with  $50 \times 50$  grid points at  $t = 0.3$  obtained by using the two different monitor functions  $G$  and  $\widehat{G}$  with  $\beta_l = \beta = 8$  and  $\gamma_l = \gamma = 1$ . It is seen from these results that the monitor  $\widehat{G}$  produces better mesh quality in terms of smoothness, skewness, and aspect ratio. The adaptive meshes and contour of the density in Fig. 6 are obtained by using  $100 \times 100$  grid points and the monitor  $\widehat{G}$ . They have a better resolution than the ones given in [28] where the monitor  $G$  is used. It also shows that the monitor  $\widehat{G}$  is successful in increasing grid concentration near contact discontinuity.

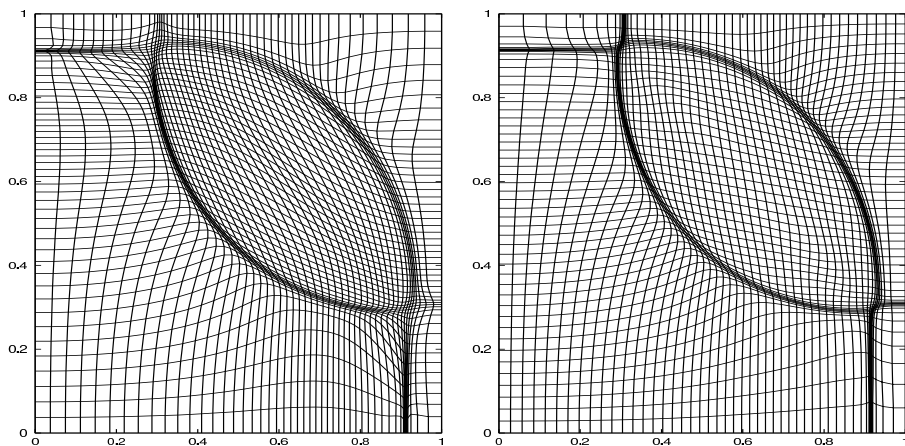


Figure 2: Example 3.1. The adaptive mesh at  $t = 0.25$ . Left:  $G$  with  $\beta = 8$  and  $\gamma = 1$ ; Right:  $\hat{G}$  with  $\beta_l = 8$  and  $\gamma_l = 1$ .

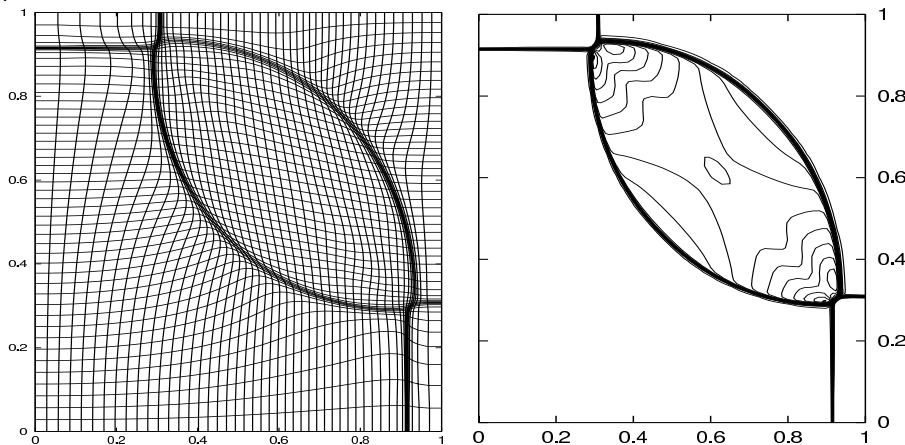


Figure 3: Example 3.1. The adaptive solutions at  $t = 0.25$  with  $50 \times 50$  grid points, obtained by using the monitor  $G$  with  $\beta = 8$  and  $\gamma = \frac{3}{2}$ . Left: adaptive mesh; Right: the density (30 equally spaced contour lines).

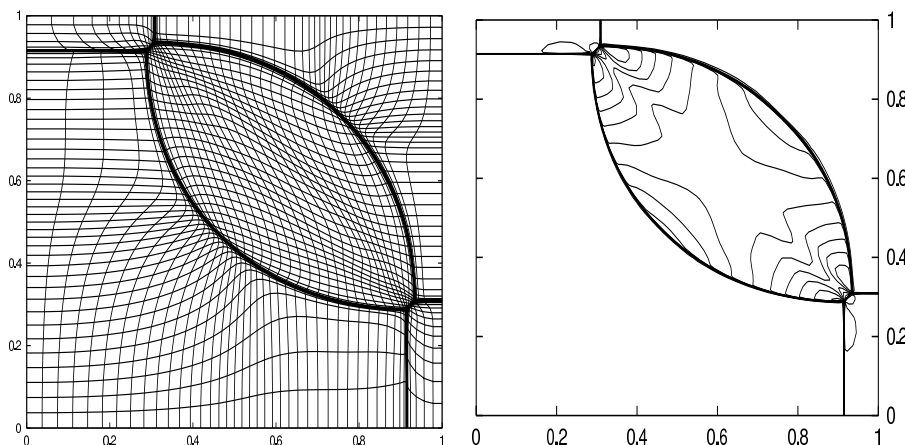


Figure 4: Same as Fig. 3, except for the monitor function  $\hat{G}$ .

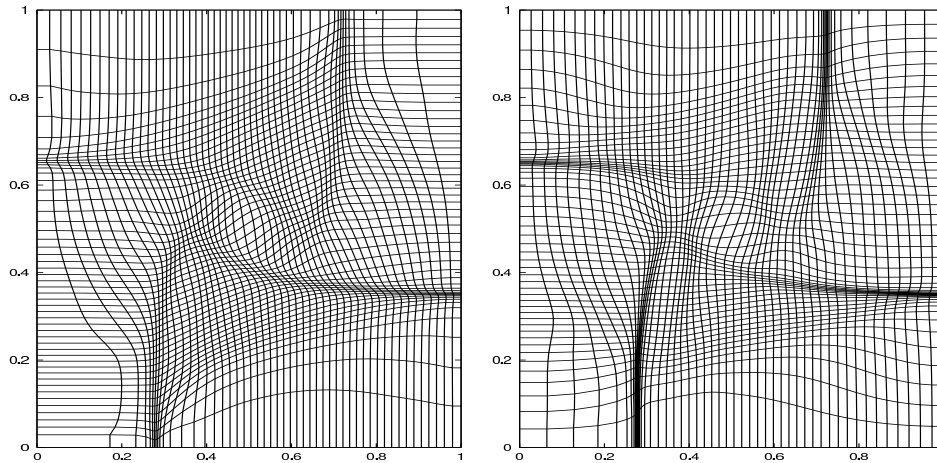


Figure 5: Example 3.2. Adaptive meshes at  $t = 0.3$  with  $50 \times 50$  grid points. Left:  $G$  with  $\beta = 8$  and  $\gamma = 1$ ; Right:  $\hat{G}$  with  $\beta_l = 8$  and  $\gamma_l = 1$ .

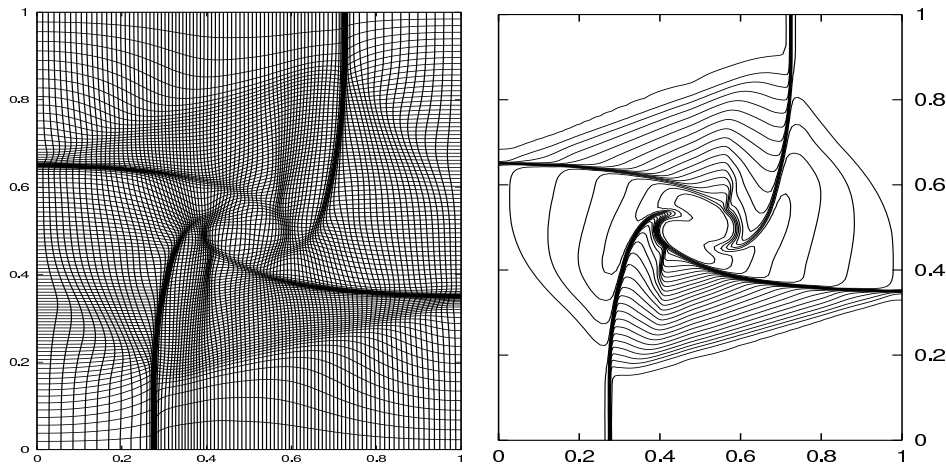


Figure 6: Example 3.2. The adaptive solutions at  $t = 0.3$  with  $100 \times 100$  grid points, obtained by using the monitor  $\hat{G}$  with  $\beta_l = 8$  and  $\gamma_l = 1$ . Left: Adaptive mesh; Right: The density (30 equally spaced contour lines).

**Example 3.3.** 2D spherical Riemann problem as given in [14].

This example is a spherical Riemann problem between two parallel walls. The main feature of the solution is the complex interactions among the waves and between waves and two walls. The problem is cylindrically symmetric within our considered time interval  $[0,0.7]$ . Hence we may solve 2D axisymmetric Euler equations, and use  $x$  to correspond to the radial coordinate. Moreover, a source term  $H = -\frac{1}{x}[\rho u, \rho u^2, \rho uv, u(E + p)]^T$  is added at the right hand side of the Euler equations (3.1).

Initially the air is at rest with the density  $\rho = 1$ , and the pressure  $p = 1$  everywhere except in a sphere centered at  $(0,0.4)$  with radius  $0.2$ . Inside the sphere, the pressure

is  $p = 5$ . The initial jump in pressure results in a strong outward moving shock wave and contact discontinuity and an inward rarefaction wave. This inward moving wave causes further a local “implosion”, and create a second outward moving shock wave. The computational domain is taken as  $[0, 1.4] \times [0, 1]$ , and the two walls are located at  $y = 0$  and  $y = 1$ . The symmetric boundary condition is used at  $x = 0$ , and free outflow is specified at  $x = 1.4$ . The reflection conditions are used at the two walls.

Figs. 7–9 show the adaptive meshes and the pressure distributions at  $t = 0.7$  by using  $G$  and  $\widehat{G}$  with  $\beta_l = \beta = 10$  and  $\gamma_l = \gamma = 1$ , respectively. A  $125 \times 100$  mesh is used for Figs. 7 and 8 and a  $250 \times 200$  mesh for Fig. 9. The flow at  $t = 0.7$  consists of several shocks and strong contact/tangential discontinuities surrounding the low density near the center of the domain. From these figures, it is observed that some main wave structures are computed with sharper resolutions. Our results in Fig. 9 can be compared with one given in [14] which is obtained using a  $600 \times 400$  mesh (Fig. 6d there). It is seen from Figs. 7 and 8 that the adaptation effect is more satisfactory with the use of the monitor  $\widehat{G}$ . The mesh is smoother in the region  $[1.2, 1.4] \times [0, 1]$ . With a fine mesh of  $250 \times 200$  grid points, the problem is well resolved, as seen in Fig. 9.

**Example 3.4.** The double-Mach reflection problem [34].

This problem was studied extensively by Woodward and Colella [34] and later by many others. We use exactly the same setup as in [34], i.e. the same initial and boundary conditions and the same solution domain  $\Omega_p = [0, 4] \times [0, 1]$ . Initially a right-moving shock with Mach 10 is positioned at the point  $(x, y) = (\frac{1}{6}, 0)$ , making a  $60^\circ$  angle with the  $x$ -axis. More precisely, the initial data are

$$U(x, y, 0) = \begin{cases} U_L, & \text{for } y \geq h(x, 0), \\ U_R, & \text{otherwise,} \end{cases}$$

where  $U = [\rho, \rho u, \rho v, E]^T$ , the left state  $U_L$ , the right state  $U_R$ , and the shock location are

$$\begin{aligned} U_L &= (8, 57.1597, -33.0012, 563.544)^T, \\ U_R &= (1.4, 0.0, 0.0, 2.5)^T, \\ h(x, t) &= \sqrt{3}(x - 1/6) - 20t. \end{aligned}$$

Figs. 10 and 11 show the adaptive meshes and contours of the density at  $t = 0.2$  with  $160 \times 80$  grid points within a cut domain  $[0, 3.1] \times [0, 1]$ . From these figures, the same phenomenon as in the previous examples is observed, although it is less obvious. Within the local regions near points  $(2.7, 0.41)$  and  $(2.6, 0.0)$ , respectively, the grid concentration obtained by  $\widehat{G}$  is better than the one given by  $G$ . Highly deformed cells have been produced by  $G$  in some local regions. Moreover, the local orthogonality of the meshes in Fig. 10 is better than one Fig. 11.

**Example 3.5.** Supersonic flows around a double ellipse configuration.

We consider a steady problem on supersonic flows around a double ellipse configuration, which is to show numerical implementation of the present adaptive moving grid algorithm

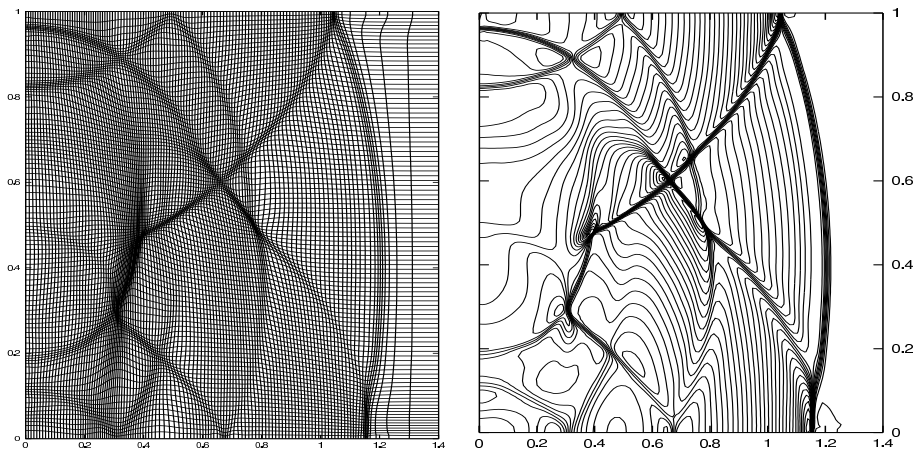


Figure 7: Example 3.3. The adaptive solutions at  $t = 0.7$  with  $125 \times 100$  grid points, obtained by using the monitor  $G$  with  $\beta = 10$  and  $\gamma = 1$ . Left: adaptive mesh; Right: the pressure (40 equally spaced contour lines).

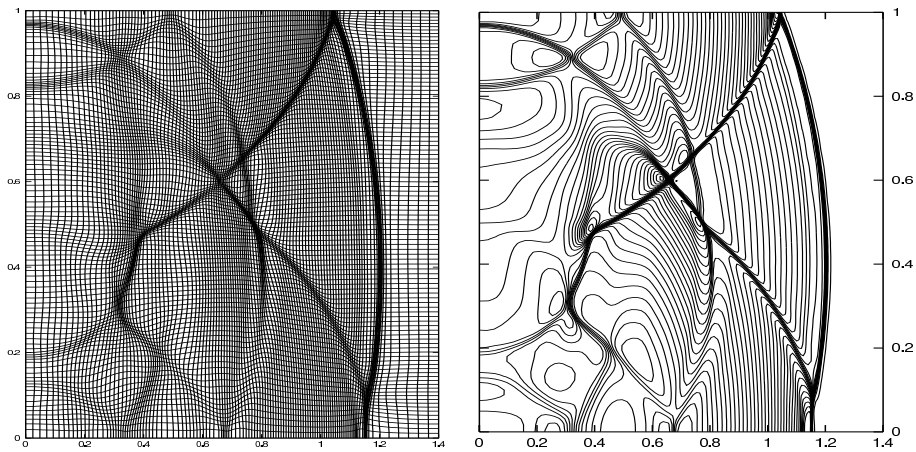


Figure 8: Same as Fig. 7, except for the monitor  $\hat{G}$ .

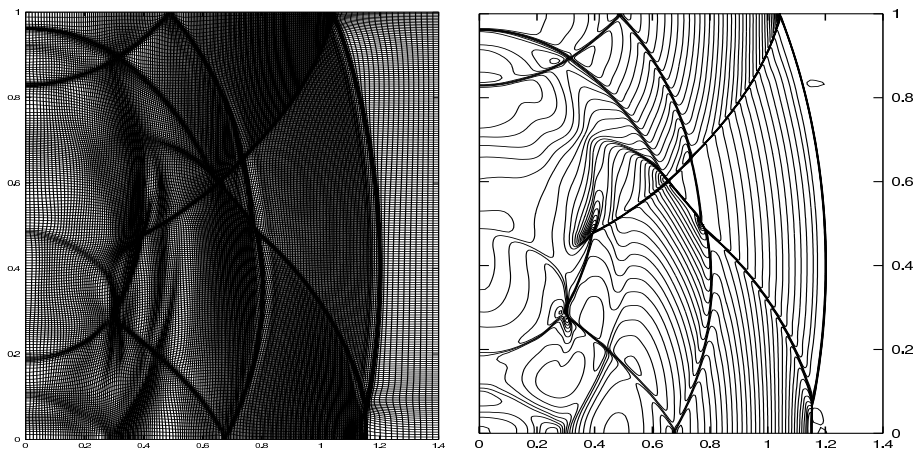


Figure 9: Same as Fig. 8 except for  $250 \times 200$  grid points.



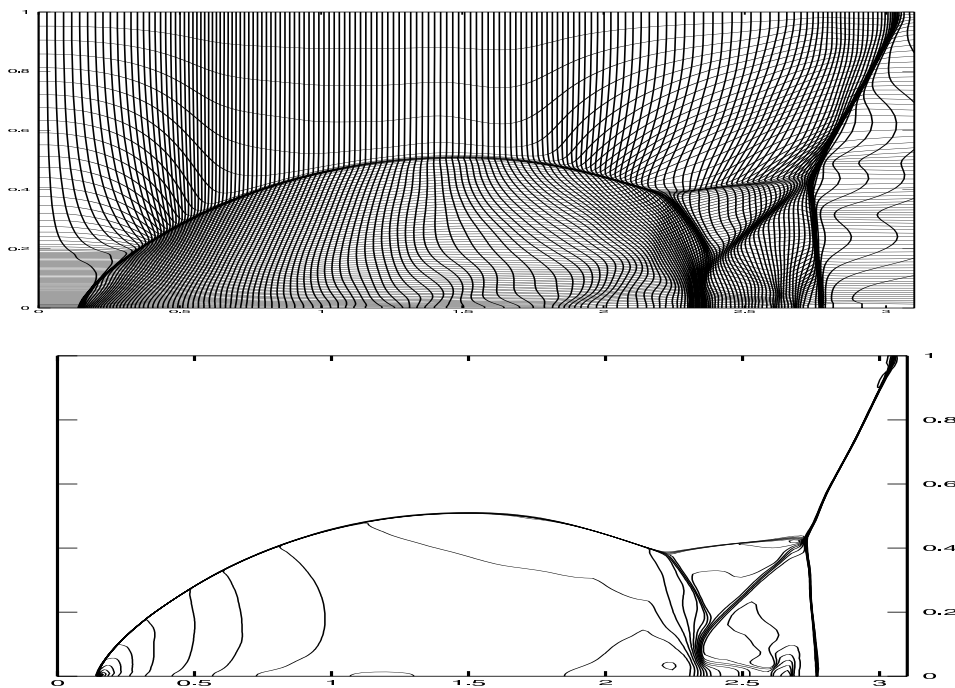


Figure 10: Example 3.4. The adaptive solutions at  $t = 0.2$  with  $160 \times 80$  grid points, obtained by using the monitor  $G$  with  $\beta = 0.6$  and  $\gamma = 1$ . Top: adaptive mesh; Bottom: the density (30 equally spaced contour lines).

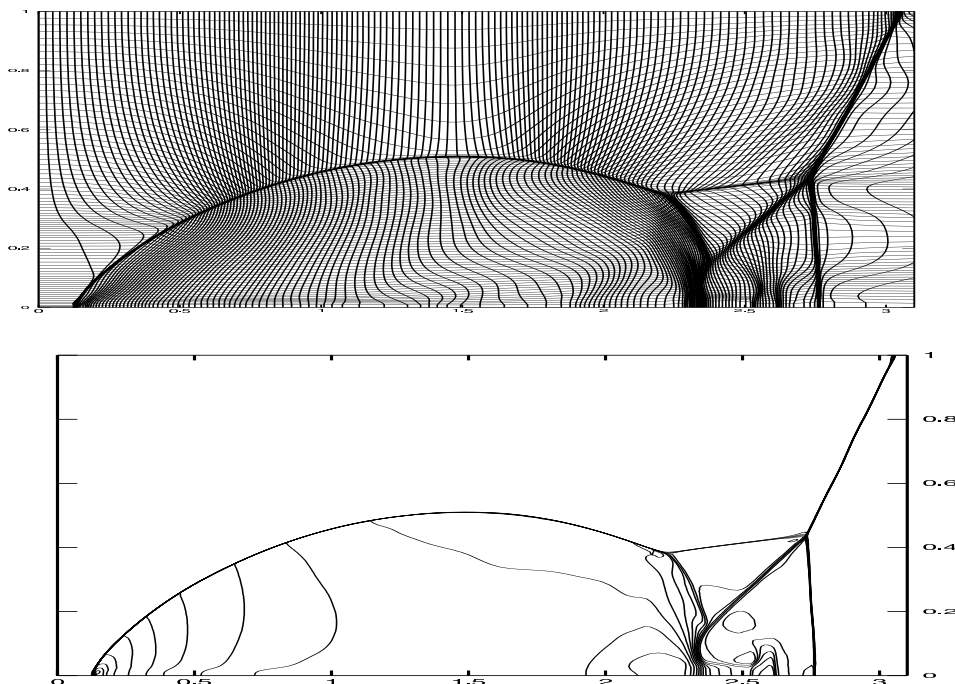


Figure 11: Same as Fig.10 except using the monitor  $\hat{G}$ .

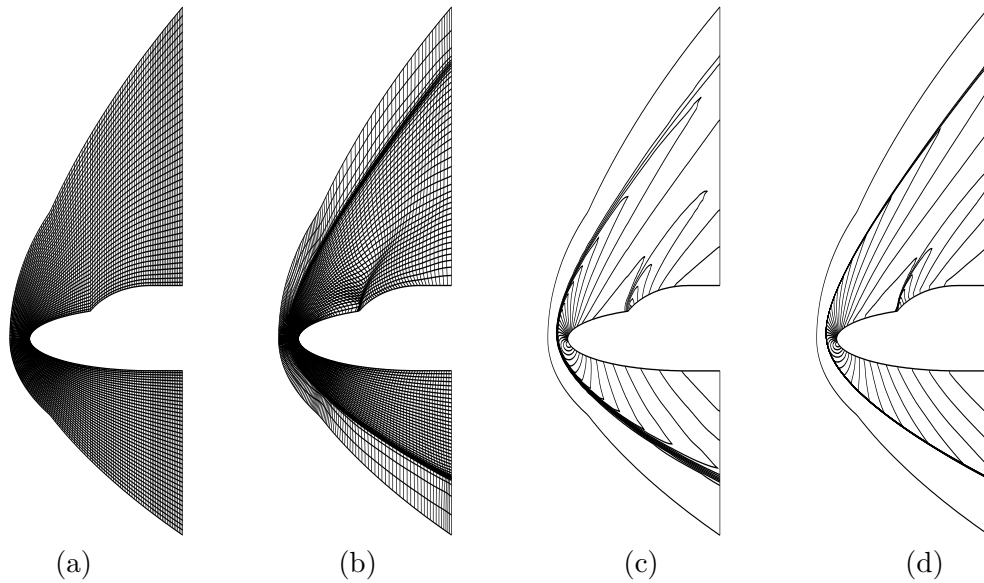


Figure 12: Example 3.5. (a): The initial mesh, (b): the adaptive mesh, with  $201 \times 41$  grid points. Also shown is the distribution of the pressures with 22 equally spaced contour lines obtained using the fixed mesh (c) and the adaptive mesh (d).

for solving the problems in a complex domain. The double ellipse configuration is defined by

$$\left(\frac{x}{0.06}\right)^2 + \left(\frac{y}{0.015}\right)^2 = 1, \quad \left(\frac{x}{0.035}\right)^2 + \left(\frac{y}{0.025}\right)^2 = 1,$$

for  $x \leq 0$ , and  $y = -0.015$  (or  $0.025$ ) in the lower (or upper) plane when  $0 \leq x \leq 0.016$ .

The problem is initialized by a free-stream with a Mach number 3 and the angle of attack  $20^\circ$ . A reflection boundary condition is imposed at the surface of the double ellipse configuration, i.e.  $k = 1$ , an inflow boundary condition is applied at the far boundary condition, i.e.  $k = N_y$ , and an outflow boundary condition is applied at  $x = 0.016$  ( $j = 1$  and  $N_x$ ). In this example, the monitor function  $\hat{G}$  is used with  $\beta_l = 0.4$  and  $\alpha_l = \gamma_l = 1$ . Since the physical domain is non-convex, we need to introduce an intermediate space  $\mathcal{D}$  like one described in Section 2.5. The computational meshes in  $\Omega_p$  and the pressure contours are shown in Figs. 12. The comparison of the results shows a significant improvement of the shock resolution.

## 4 Concluding remarks

In this paper, we have further studied the adaptive moving mesh method proposed in [28] for computations of the Euler equations in fluid dynamics. Our adaptive mesh algorithm includes two parts: PDE evolution and mesh redistribution. The first part is an appropriate high resolution finite volume scheme, and the second part is an iterative procedure

including redistribution of grid points and a conservative solution–interpolation. Because the two parts are decoupled, the present algorithm may be extended to three-dimensional Euler flow calculations following Tang and Tang [29].

The monitor function is one of the most important elements in the moving mesh algorithms. The appropriate choice of the monitor will produce grids with good quality in terms of smoothness, skewness, and aspect ratio. The conventional monitor functions usually depend on the magnitude of the gradient of the solutions, which may not be always effective to increase the grid concentration in the local regions containing shock waves and contact discontinuities or their interactions. To improve the performance of the adaptive method, a directional monitor function has been proposed in this work. Although the monitor function is defined based on the dimension-splitting idea, it is different from the existing multidimensional-equidistribution approaches. The latter is just a direct tensor-product extension of the 1D equidistribution scheme.

We have also presented some numerical computations for several test problems and numerical comparisons. The results show that the new monitor function is more effective than the monitor used in [28], which improves the resolution of the discontinuities, by clustering more grid points within the regions containing shocks and contact discontinuities. However, the choices of the different parameters in the monitor functions depend strongly on the computed problem, when we expect to present a “satisfactory” or “optimal” result. It is very important to further improve the present algorithm in order to reduce this dependence. A possible and good direction is to use the monitor function given in the recent paper of Zegeling, de Boer, and Tang [36].

## Acknowledgments

The author would like to thank Professors Tao Tang and Paul Zegeling for numerous discussions during the preparation of this work. This research is partially supported by the National Basic Research Program under the Grant 2005CB321703, the National Natural Science Foundation of China (No. 10431050, 10576001), Laboratory of Computational Physics, and SRF for ROCS, SEM.

## References

- [1] B. N. Azarenok, S. A. Ivanenko and T. Tang, Adaptive mesh redistribution method based on Godunov’s scheme, *Commun. Math. Sci.*, 1 (2003), 152-179.
- [2] G. J. Ball, A free-Lagrange method for unsteady compressible flow: Simulation of a confined cylindrical blast wave, *Shock Waves*, 5 (1996), 311–325.
- [3] J. U. Brackbill, An adaptive grid with directional control, *J. Comput. Phys.*, 108 (1993), 38-50.
- [4] J. U. Brackbill and J. S. Saltzman, Adaptive zoning for singular problems in two dimensions, *J. Comput. Phys.*, 46 (1982), 342–368.
- [5] W. M. Cao, W. Z. Huang and R. D. Russell, A study of monitor functions for two–dimensional adaptive mesh generation, *SIAM J. Sci. Comput.*, 20 (1999), 1978–1999.

- [6] W. M. Cao, W. Z. Huang and R. D. Russell, An  $r$ -adaptive finite element method based upon moving mesh PDEs, *J. Comput. Phys.*, 149 (1999), 221–244.
- [7] H. D. Ceniceros and T. Y. Hou, An efficient dynamically adaptive mesh for potentially singular solutions, *J. Comput. Phys.*, 172 (2001), 609-639.
- [8] S. F. Davis and J. E. Flaherty, An adaptive finite element method for initial-boundary value problems for partial differential equations, *SIAM J. Sci. Stat. Comput.*, 3 (1982), 6-27.
- [9] A. S. Dvinsky, Adaptive grid generation from harmonic maps on Riemannian manifolds, *J. Comput. Phys.*, 95 (1991), 450–476.
- [10] R. Fazio and R. LeVeque, Moving-mesh methods for one-dimensional hyperbolic problems using CLAWPACK, *Comp. Math. Appl.*, 45 (2003), 273-298.
- [11] A. Harten and J. M. Hyman, Self-adjusting grid methods for one-dimensional hyperbolic conservation laws, *J. Comput. Phys.*, 50 (1983), 235–269.
- [12] C. W. Hirt, A. A. Amsden and J. L. Cook, An arbitrary Lagrangian-Eulerian computing method for all flow speeds, *J. Comput. Phys.*, 14 (1974), 227-253; 135 (1997), 203-216.
- [13] W. H. Hui, P. Y. Li and Z. W. Li, A unified coordinate system for solving the two-dimensional Euler equations, *J. Comput. Phys.*, 153 (1999), 596-637.
- [14] J. O. Langseth and R. J. LeVeque, A wave propagation method for three-dimensional hyperbolic conservation laws, *J. Comput. Phys.*, 165 (2000), 126–166.
- [15] P. D. Lax and X. D. Liu, Solutions of two-dimensional Riemann problems of gas dynamics by positive schemes, *SIAM J. Sci. Comput.*, 19 (1998), 319–340.
- [16] R. Li, T. Tang and P. W. Zhang, Moving mesh methods in multiple dimensions based on harmonic maps, *J. Comput. Phys.*, 170 (2001), 562-588.
- [17] R. Li, T. Tang, and P. W. Zhang, A moving mesh finite element algorithm for singular problems in two and three space dimensions, *J. Comput. Phys.*, 177 (2002), 365-393.
- [18] S. Li and L. Petzold, Moving mesh methods with upwinding schemes for time-dependent PDEs, *J. Comput. Phys.*, 131 (1997), 368-377.
- [19] V. D. Liseikin, *Grid Generation Methods*, Springer, 1999.
- [20] F. Liu, S. Ji and G. Liao, An adaptive grid method and its application to steady Euler flow calculations, *SIAM J. Sci. Comput.*, 20 (1998), 811-825.
- [21] K. Miller and R. N. Miller, Moving finite element. I, *SIAM J. Numer. Anal.*, 18 (1981), 1019–1032.
- [22] R. B. Pember and R. W. Anderson, A comparison of staggered-mesh Lagrange plus remap and cell-centered direct Eulerian Godunov schemes for Eulerian shock hydrodynamics, Lawrence Livermore National Laboratory, CA, UCRL-JC-139820, 1998.
- [23] K. Saleri and S. Steinberg, Flux-corrected transport in a moving grid, *J. Comput. Phys.*, 111 (1994), 24-32.
- [24] C. W. Schulz-Rinne, J. P. Collins and H. M. Glaz, Numerical solution of the Riemann problem for two-dimensional gas dynamics, *SIAM J. Sci. Comput.*, 14 (1993), 1394–1414.
- [25] C.-W. Shu and S. Osher, Efficient implementation of essentially non-oscillatory shock-capturing schemes, *J. Comput. Phys.*, 77 (1988), 439-471.
- [26] J. M. Stockie, J. A. Mackenzie and R. D. Russell, A moving mesh method for one-dimensional hyperbolic conservation laws, *SIAM J. Sci. Comput.*, 22 (2001), 1791-1813.
- [27] J. F. Thompson, B. K. Soni and N. P. Weatherill, *Handbook of Grid Generation*, CRC Press, Boca Raton, London, New York, Washington, D.C., 1999.
- [28] H. Z. Tang and T. Tang, Adaptive mesh methods for one- and two-dimensional hyperbolic conservation laws, *SIAM J. Numer. Anal.*, 41 (2003), 487-515.
- [29] H. Z. Tang and T. Tang, Multi-dimensional moving mesh methods for shock computations,

- in: S. Y. Cheng, C.- W. Shu and T. Tang (Eds.), *Recent Advances in Scientific Computing and Partial Differential Equations*, Contemporary Mathematics, volume 330, AMS, 2003, pp. 169-183.
- [30] H. Z. Tang, T. Tang and P. W. Zhang, An adaptive mesh redistribution method for nonlinear Hamilton-Jacobi equations in two- and three-dimensions, *J. Comput. Phys.*, 188 (2003), 534-572.
- [31] T. Tang, Moving mesh methods for computational fluid dynamics, in: Z.-C. Shi, Z. Chen, T. Tang and D. Yu (Eds.), *Recent Advances in Adaptive Computation*, Contemporary Mathematics, volume 383, AMS, 2005, pp. 141-173.
- [32] B. van Leer, Towards the ultimate conservative difference scheme, V. A second order sequel to Godunov's method, *J. Comput. Phys.*, 32 (1979), 101-136.
- [33] A. Winslow, Numerical solution of the quasi-linear Poisson equation, *J. Comput. Phys.*, 1 (1967), 149-172.
- [34] P. Woodward and P. Colella, The numerical simulation of two dimensional fluid flow with strong shocks, *J. Comput. Phys.*, 54 (1984), 115-173.
- [35] P. A. Zegeling, On resistive MHD models with adaptive moving meshes, *J. Sci. Comput.*, 24 (2005), 263-284.
- [36] P. A. Zegeling, W. D. de Boer and H. Z. Tang, Robust and efficient adaptive moving mesh solution of the 2-D Euler equations, in: Z.-C. Shi, Z. Chen, T. Tang and D. Yu (Eds.), *Recent Advances in Adaptive Computation*, Contemporary Mathematics, volume 383, AMS, 2005, pp. 375-368.